New Journal of Physics
The open access journal at the forefront of physics

Deutsche Physikalische Gesellschaft DPG
IOP Institute of Physics

Published in partnership with: Deutsche Physikalische Gesellschaft and the Institute of Physics

OPEN ACCESS

RECEIVED
24 August 2017

REVISED
20 October 2017

ACCEPTED FOR PUBLICATION
17 November 2017

PUBLISHED
22 January 2018

PAPER

Extremely correlated Fermi liquid theory of the *t-J* model in 2 dimensions: low energy properties

B Sriram Shastry and Peizhi Mai

Physics Department, University of California, Santa Cruz, CA 95064, United States of America

E-mail: sriram@physics.ucsc.edu

Keywords: strong correlations, 2-dimensional *t-J* model, temperature dependent resistivity, cotangent Hall angle, extremely correlated Fermi liquid

Abstract

Low energy properties of the metallic state of the two-dimensional *t-J* model are presented for second neighbor hopping with hole-doping ($t' \leqslant 0$) and electron-doping ($t' > 0$), with various super-exchange energy *J*. We use a closed set of equations for the Greens functions obtained from the *extremely correlated Fermi liquid theory*. These equations reproduce the known low energies features of the large *U* Hubbard model in infinite dimensions. The density and temperature dependent quasiparticle weight, decay rate and the peak spectral heights over the Brillouin zone are calculated. We also calculate the resistivity, Hall conductivity, Hall number and cotangent Hall angle. The spectral features display high thermal sensitivity at modest *T* for density $n \gtrsim 0.8$, implying a suppression of the effective Fermi-liquid temperature by two orders of magnitude relative to the bare bandwidth. The cotangent Hall angle exhibits a T^2 behavior at low *T*, followed by an interesting kink at higher *T*. The Hall number exhibits strong renormalization due to correlations. Flipping the sign of t' changes the curvature of the resistivity versus *T* curves between convex and concave. Our results provide a natural route for understanding the observed difference in the temperature dependent resistivity of strongly correlated electron-doped and hole-doped matter.

1. Introduction

The *t-J* model in 2-dimensions (2d) has been argued to be of fundamental importance for understanding strongly correlated matter, including the high T_c superconductors [1, 2]. Due to the difficulties inherent in the strong coupling problem, very few techniques are available for extracting its low temperature physics. Towards this end we have recently developed the *extremely correlated Fermi liquid* (ECFL) theory [3, 4]. It is an analytical method for treating very strong correlations of lattice Fermions, employing Schwinger's technique of functional differential equations togather with several important added ingredients. While further details can be found in [3, 4], a brief summary of the main idea behind the ECFL theory seems appropriate. We consider the Hubbard model with a large interaction $U \to \infty$, and hence the name of the theory. A well known expansion in the inverse powers of *U* leads to the *t-J* model (defined below [2]). Taking the infinite *U* limit forces one to abandon the conventional Feynman diagram based perturbation theory in *U*, and to make a fresh start. The ECFL theory starts with the graded Lie-algebra of the Gutzwiller projected, i.e. infinite-*U* limit Fermi operators equations (2), (3). This leads to an exact functional differential equation for the Greens functions, known as the Schwinger equation of motion equation (18) or (22). In this equation, a parameter λ is introduced; λ is bounded in the range $\in [0,\ 1]$ and represents the evolution from the free Fermi limit. We then use a systematic expansion in the parameter λ, for solving the Schwinger equations perturbatively in λ. In this scheme we start with the uncorrelated Fermi gas at $\lambda = 0$ and end up at the fully correlated projected Fermion problem at $\lambda = 1$. The scheme thus represents a generalization of the usual perturbation theory for canonical Fermionic models, in order to handle a non-canonical Fermionic problem such as the *t-J* model. The context of interacting Bosons provides a useful parallel. In the well known problem of representing spin *S* variables in terms of canonical Bosons, one uses the expansion parameter $\frac{1}{2S}$ with a similar range $\frac{1}{2S} \in [0,\ 1]$. We may think of λ as being

analogous to the parameter $\frac{1}{2S}$ as shown in [4]. The introduction of the parameter λ and the λ-expansion scheme thus enabled are among the main technical advances introduced in the ECFL theory.

This approach has been recently benchmarked [5–7] against the numerically exact results from the single impurity Anderson model, and the $d = \infty$ Hubbard model from dynamical mean field theory (DMFT) [8, 9]. These tests provide quantitative support to our general scheme described below, especially for low energy response. Our scheme has no specific limitation to $d = \infty$, and is expected to be reasonably accurate in any dimension $d > 1$, including 2 dimensions, a case of great experimental importance due to the High T_c cuprate materials. It is applied here to probe the metallic state of the *t-J* model in 2d. We present results for the electron self energy, the spectral functions, the resistivity the Hall constant and the Hall angle at various temperatures and electron density $n = N/N_s$ (number of electrons per site). We also frequently use the notation of hole density $\delta = (1 - n)$ (in addition to n), following the convention used in several experimental studies of doped Mott systems.

We explore various values of the parameters of the *t-J* model, including the second neighbor hopping, which turns out to play a very important role in determining the effective Fermi liquid (FL) temperature scale. We investigate the resistivity due to mutual collisions of electrons at low temperatures, and its dependence on the parameters of the model. We pay special attention to the resistivity since this easily measured—but notoriously hard to calculate object, reveals the lowest energy scale physics of charge excitations in metallic systems, and therefore is of central importance.

2. Methods

In this section we summarize the equations used in the present calculation, together with the arguments leading to them- further details may be found in earlier papers on this theory [3, 5–7]. In section 2.1 the model is defined and the exact Schwinger–Dyson equations of motion (EOM) are written out. In section 2.2 the λ parameter is introduced and the exact factorization of the Greens function into an auxiliary Greens function and a caparison function are noted. In section 2.3 we summarize the shift identities of the *t-J* model. The shift transformation is a simple and yet important invariance of the *t-J* model leading to important constraints on possible approximations. Within the λ expansion, this invariance obligates the introduction of a second chemical potential u_0, which is then treated as a Lagrange multiplier to be fixed through sum-rules. In section 2.4 we collect the equations of the second order theory. In section 2.5 we summarize the rationale for a high energy cutoff of the equations given in section 2.4.

2.1. The *t-J* model preliminaries

The *t-J* model is a two component Fermi system on a lattice, defined on the restricted subspace of three local states, obtained by excluding all doubly occupied configurations. The allowed states at a single site are $|a\rangle$ with $a = 0, \uparrow, \downarrow$, and the double occupancy state $|\uparrow\downarrow\rangle$ is removed by the (Gutzwiller) projection operator $P_{\rm G} = \Pi_i(1 - n_{i\uparrow}n_{i\downarrow})$. We use the Hubbard operators $X_i^{a,b} = |a\rangle\langle b|$, which are expressible in terms of the usual Fermions $C_{i\sigma}$, $C_{i\sigma}^\dagger$ and the Gutzwiller projector $P_{\rm G}$ as:

$$X_i^{\sigma 0} = P_{\rm G} C_{i\sigma}^\dagger P_{\rm G};\quad X_i^{0\sigma} = P_{\rm G} C_{i\sigma} P_{\rm G};\quad X_i^{\sigma\sigma'} = P_{\rm G} C_{i\sigma}^\dagger C_{i\sigma'} P_{\rm G}. \tag{1}$$

These obey the anti-commutation relations

$$\{X_i^{0\sigma_i}, X_j^{\sigma_j 0}\} = \delta_{i,j}(\delta_{\sigma_i,\sigma_j} - \sigma_i\sigma_j X_i^{\bar{\sigma}_i,\bar{\sigma}_j}) \tag{2}$$

and the commutators

$$[X_i^{0\sigma_i}, X_j^{\sigma_j\sigma_k}] = \delta_{ij}\delta_{\sigma_i\sigma_j} X_i^{0\sigma_k};\quad [X_i^{\sigma_i 0}, X_j^{\sigma_j\sigma_k}] = -\delta_{ij}\delta_{\sigma_i\sigma_k} X_i^{\sigma_j 0}. \tag{3}$$

The Hamiltonian of the general *t-J* model H_{tJ} is

$$\begin{aligned} H_{tJ} &= H_t + H_J, \\ H_t &= -\sum_{ij} t_{ij} X_i^{\sigma 0} X_j^{0\sigma} - \boldsymbol{\mu}\sum_i X_i^{\sigma\sigma};\quad H_J = \frac{1}{2}\sum_{ij} J_{ij}\left(\vec{S}_i.\vec{S}_j - \frac{1}{4}X_i^{\sigma\sigma}X_j^{\sigma'\sigma'}\right), \end{aligned} \tag{4}$$

where we sum over repeated spin indices. Here $\boldsymbol{\mu}$ is the chemical potential and the spin is given in terms of the Fermions and the Pauli matrices $\vec{\tau}$ as usual $\vec{S} = \frac{1}{2}X_i^{\sigma 0}\vec{\tau}_{\sigma\sigma'}X_i^{0\sigma'}$. We will restrict in the following to nearest neighbor exchange J, and first (t) and second neighbor (t') hopping on a square lattice.

For the purpose of computing the Green's functions we add Schwinger sources to the Hamiltonian; the commuting (Bosonic) potential $\mathcal{V}$ couples to the charge as well as spin density. These sources serve to generate compact Schwinger EOM, and are set to zero at the end. The zero source equations are usually termed as the Schwinger–Dyson equations. In that limit we recover spatial and temporal translation invariance of the Greens

function. Explicitly we write

$$\hat{\mathcal{A}}_S = \sum_i \int_0^\beta \hat{\mathcal{A}}_S(i,\tau)\mathrm{d}\tau; \quad \hat{\mathcal{A}}_S(i,\tau) = \mathcal{V}_i^{\sigma'\sigma}(\tau)X_i^{\sigma'\sigma}(\tau) \tag{5}$$

and all time dependences are as in $Q(\tau) = \mathrm{e}^{\tau H_{tJ}} Q \mathrm{e}^{-\tau H_{tJ}}$. The generating functional of Green's functions of the *t-J* model is

$$Z[\mathcal{V}] \equiv \mathrm{Tr}_{tJ}\ \mathrm{e}^{-\beta H_{tJ}} T_\tau(\mathrm{e}^{-\hat{\mathcal{A}}_S}). \tag{6}$$

It reduces to the standard partition function on turning off the indicated source terms the Green's functions for positive times $0 \leqslant \tau_j \leqslant \beta$, are defined as usual:

$$\mathcal{G}_{\sigma\sigma'}(i\tau_i, f\tau_f) = -\langle T_\tau(\mathrm{e}^{-\hat{\mathcal{A}}_S} X_i^{0\sigma}(\tau_i) X_f^{\sigma' 0}(\tau_f))\rangle, \tag{7}$$

where for an arbitrary $\mathcal{Q}$ we define

$$\langle \mathcal{Q}\rangle \equiv \frac{1}{Z}\mathrm{Tr}_{tJ}\ \mathrm{e}^{-\beta H_{tJ}} T_\tau(\mathrm{e}^{-\hat{\mathcal{A}}_S}\mathcal{Q}\,). \tag{8}$$

We note that n_σ, the number of particles per site, is determined from the number sum rule:

$$n_\sigma = \mathcal{G}_{\sigma\sigma}(i\tau^-, i\tau) \tag{9}$$

and $\boldsymbol{\mu}$ the chemical potential is fixed by this constraint. By taking the time derivative of equation (7) we see that the Green's function satisfies the EOM

$$\partial_{\tau_i}\mathcal{G}_{\sigma_i\sigma_f}(i,f) = -\delta(\tau_i-\tau_f)\delta_{if}(1-\gamma_{\sigma_i\sigma_f}(i\tau_i)) - \langle T_\tau(\mathrm{e}^{-\hat{\mathcal{A}}_S}[H_{tJ}+\hat{\mathcal{A}}_S(i,\tau_i), X_i^{0\sigma_i}(\tau_i)]\ X_f^{\sigma_f 0}(\tau_f))\rangle, \tag{10}$$

where the local Green's function is defined as

$$\gamma_{\sigma_a\sigma_b}(i\tau_i) = \sigma_a\sigma_b\mathcal{G}_{\bar{\sigma}_b\bar{\sigma}_a}(i\tau_i^-, i\tau_i), \tag{11}$$

with the notation

$$\bar{\sigma}_i = -\sigma_i. \tag{12}$$

Using the Hamiltonian equation (4) and canonical relations equations (2), (3) we find

$$[H_{tJ}, X_i^{0\sigma_i}] = \sum_j t_{ij}X_j^{0\sigma_i} + \boldsymbol{\mu}X_i^{0\sigma_i} - \sum_{j\sigma_j} t_{ij}(\sigma_i\sigma_j)X_i^{\bar{\sigma}_i\bar{\sigma}_j}\ X_j^{0\sigma_j} + \frac{1}{2}\sum_{j\neq i} J_{ij}\ (\sigma_i\sigma_j)X_j^{\bar{\sigma}_i\bar{\sigma}_j}X_i^{0\sigma_j} \tag{13}$$

and

$$[\hat{\mathcal{A}}_S(i\tau_i), X_i^{0\sigma_i}] = -\mathcal{V}_i^{\sigma_i\sigma_j}X_i^{0\sigma_j}. \tag{14}$$

Substituting into equation (10) and using the free Fermi gas Green's function:

$$\mathbf{g}^{-1}_{0,\sigma_i\sigma_j}(i\tau_i, j\tau_j) = \{\delta_{\sigma_i\sigma_j}[\delta_{ij}(\boldsymbol{\mu}-\partial_{\tau_i}) + t_{ij}] - \delta_{ij}\mathcal{V}_i^{\sigma_i\sigma_j}(\tau_i)\}\delta(\tau_i-\tau_j), \tag{15}$$

we obtain

$$\begin{aligned}\mathbf{g}^{-1}_{0,\sigma_i\sigma_j}(i\tau_i, j\tau_j)\mathcal{G}_{\sigma_j\sigma_f}(j\tau_j, f\tau_f) &= \delta(\tau_i-\tau_f)\delta_{if}(1-\gamma_{\sigma_i\sigma_f}(i\tau_i))\\ -\sum_{j\sigma_j} t_{ij}(\sigma_i\sigma_j)\ \langle T_\tau(X_i^{\bar{\sigma}_i\bar{\sigma}_j}(\tau_i)X_j^{0\sigma_j}(\tau_i)\ X_f^{\sigma_f 0}(\tau_f))\rangle &+ \frac{1}{2}\sum_{k\sigma_j} J_{ik}(\sigma_i\sigma_j)\langle T_\tau(X_k^{\bar{\sigma}_i\bar{\sigma}_j}(\tau_i)X_i^{0\sigma_j}(\tau_i)X_f^{\sigma_f 0}(\tau_f)).\end{aligned} \tag{16}$$

We next 'reduce' the higher order Green's function to a lower one using the identity (valid for any operator $\mathcal{Q}$):

$$\langle T_\tau X_i^{\sigma\sigma'}(\tau)\,\mathcal{Q}\rangle = \langle T_\tau X_i^{\sigma\sigma'}(\tau)\rangle\ \langle T_\tau\,\mathcal{Q}\rangle - \frac{\delta}{\delta\mathcal{V}_i^{\sigma\sigma'}(\tau)}\langle T_\tau\,\mathcal{Q}\rangle \tag{17}$$

and rearranging terms we obtain the fundamental Schwinger EOM:

$$(\mathbf{g}^{-1}_{0,\sigma_i\sigma_j}(i\tau_i, j\tau_j) - \hat{X}_{\sigma_i\sigma_j}(i\tau_i, j\tau_j) - Y_{1\sigma_i\sigma_j}(i\tau_i, j\tau_j)) \times \mathcal{G}_{\sigma_j\sigma_f}(j\tau_j, f\tau_f) = \delta_{if}\delta(\tau_i-\tau_f)(\delta_{\sigma_i\sigma_f} - \gamma_{\sigma_i\sigma_f}(i\tau_i)), \tag{18}$$

where we defined the functional derivative operator at site i and time τ_i

$$D_{\sigma_i\sigma_j}(i\tau_i) = \sigma_i\sigma_j\frac{\delta}{\delta\mathcal{V}_i^{\bar{\sigma}_i\bar{\sigma}_j}(\tau_i)}, \tag{19}$$

the composite derivative operator

$$\hat{X}_{\sigma_i\sigma_j}(i\tau_i, j\tau_j) = \delta(\tau_i-\tau_j) \times \left(-t_{ij}D_{\sigma_i\sigma_j}(i\tau_i) + \delta_{ij}\sum_k \frac{1}{2}J_{ik}D_{\sigma_i\sigma_j}(k\tau_i)\right) \tag{20}$$

and corresponding Y_1 as

$$Y_{1\sigma_i\sigma_j}(i\tau_i,\, j\tau_j) = -\delta(\tau_i - \tau_j) \times \left(-t_{ij}\gamma_{\sigma_i\sigma_j}(i\tau_i) + \delta_{ij}\sum_k \frac{1}{2} J_{ik}\gamma_{\sigma_i\sigma_j}(k\tau_i) \right). \tag{21}$$

By considering the spin, space and time variables as generalized matrix indices, we can symbolically write equation (18) as

$$(\mathbf{g}_0^{-1} - \hat{X} - Y_1)\,.\,\mathcal{G} = \delta\ (\mathbb{1} - \gamma). \tag{22}$$

2.2. The λ expansion and the auxiliary Greens function

The main task is to compute solutions of the Schwinger–Dyson equation, i.e. the functional differential equation (18) or (22). If symmetry-breaking, such as magnetism or superconductivity is ignored, then a liquid state ensues, where we would like the solution to connect continuously with the Fermi gas. For this purpose we seek guidance from standard Feynman–Dyson perturbation theory for canonical models. The repulsive Hubbard model is an ideal example, where the corresponding Schwinger–Dyson equation can be schematically written as:

$$(\mathbf{g}_0^{-1} - U\delta/\delta\mathcal{V} - UG)\ .\ G = \delta\ \mathbb{1}. \tag{23}$$

Comparing with equation (22), we see that the left-hand sides are of the same form, but the right-hand sides differ, in equation (22) the local Greens function γ multiplies the delta function. In turn this extra term originates from the second (non canonical) term in the anti-commutator in equation (2), and is therefore the signature term of extremely strong correlations.

Within the Schwinger viewpoint of equation (23), we can view the skeleton graph perturbation theory (Feynman–Dyson) as an iterative scheme in U, i.e. using the nth order results to generate the $(n+1)$th order terms by functional differentiation. In the ECFL theory the iterative scheme used is defined by generalizing equation (22) to

$$(\mathbf{g}_0^{-1} - \lambda\hat{X} - \lambda Y_1)\,.\,\mathcal{G} = \delta\ (\mathbb{1} - \lambda\gamma). \tag{24}$$

The explicit solutions in the ECFL theory start from this basic equation. More explicitly, in equation (24) the exact equation (18) is generalized to include the λ parameter[1] by scaling $\hat{X}_{\sigma_i\sigma_j},\ Y_{i\sigma_i\sigma_j},\ \gamma_{\sigma_i\sigma_j} \to \lambda\hat{X}_{\sigma_i\sigma_j},\ \lambda Y_{i\sigma_i\sigma_j},\ \lambda\gamma_{\sigma_i\sigma_j}$. The starting point for the iteration is $\lambda = 0$, corresponding to the Fermi gas. As we iterate towards $\lambda = 1$, equation (24) reduces to the exact equation equation (22). The Gutzwiller projection is fully effective only at the end point of the iterative scheme $\lambda = 1$, while for intermediate values of λ, we have only a partial reduction of the number of doubly occupied sites. The role of U in equation (23) is roughly similar, at $U = 0$ we have the Fermi gas, which evolves into an interacting theory with increasing U, giving us the Feynman–Dyson perturbation theory. The range of λ ($\in[0,\ 1]$) in equation (24) is bounded above, as opposed to that of $U \in [0,\ \infty]$ in equation (23). Therefore the ECFL theory avoids dealing with a major headache of the canonical theory whenever a coupling constant becomes large. Recall that realistic interactions in correlated matter usually involve a large coupling parameter U. For this purpose one is forced to make hard-to-control approximations, such as summing specific classes of diagrams in different parameter ranges. The introduction of λ into the ECFL equations opens the possibility that a low order calculation might suffice to give accurate results at low excitation energies. This possibility is in-fact realized for important strong coupling problems as shown earlier [5].

We found in [3] that an efficient method for proceeding with the iterative scheme is to first perform a factorization of the Greens function into two parts. The first is an auxiliary Greens function $\mathbf{g}$ satisfying a canonical equation, thus admitting a Dysonian expansion with its attendant advantage of summing a geometric series with every added term of the denominator. There remain some terms that cannot be pushed into the denominator, these are collected together as the caparison function $\widetilde{\mu}$. In the matrix notation used above we first decompose the Greens function as:

$$\mathcal{G} = \mathbf{g}\,.\,\widetilde{\mu}, \tag{25}$$

this implies a product in the $\vec{k},\ \omega$ domain as written below in equation (32). The differential operator X in equation equation (24) is distributed over the two factors of equation (25) using the Leibniz product rule, as

$$X.\mathbf{g}.\widetilde{\mu} = \overbrace{X.\mathbf{g}}.\widetilde{\mu} + \overbrace{X.\mathbf{g}.\widetilde{\mu}} \tag{26}$$

[1] In [4] we have noted an important generalization of these commutators to include a continuous parameter $\lambda \in [0,\ 1]$, thus defining the so called λ fermions. Using them one can systematically obtain the λ expansion encountered below from these relations directly. Here we stick to a simpler description with λ introduced by hand, in the EOM below.

where the contraction symbol $\overrightarrow{Xa}$ indicates the term being differentiated by the functional derivative terms in X, while the matrix indices follow the dots. Using $\mathbf{g}^{-1}.\mathbf{g} = \mathbb{1}$ equation (24) is now written as

$$(\mathbf{g}_0^{-1} - \lambda\overrightarrow{X}.\mathbf{g}.\mathbf{g}^{-1} - \lambda Y_1).\mathbf{g}.\widetilde{\mu} = \delta\ (\mathbb{1} - \lambda\gamma) + \lambda\overrightarrow{X.\mathbf{g}.\widetilde{\mu}}. \tag{27}$$

This equation factors exactly into two equations upon insisting that $\mathbf{g}$ has a canonical structure:

$$(\mathbf{g}_0^{-1} - \lambda\overrightarrow{X}.\mathbf{g}.\mathbf{g}^{-1} - \lambda Y_1) = \mathbf{g}^{-1} \tag{28}$$

and

$$\widetilde{\mu} = \delta\ (\mathbb{1} - \lambda\gamma) + \lambda\overrightarrow{X.\mathbf{g}.\widetilde{\mu}}. \tag{29}$$

We can then use $\mathbf{g}.\mathbf{g}^{-1} = \mathbb{1}$ to simplify the term $\overrightarrow{X}.\mathbf{g}.\mathbf{g}^{-1} = -\overrightarrow{X.\mathbf{g}.\mathbf{g}^{-1}}$, giving rise to a Dyson self-energy expressed in terms of a Dyson vertex function. The idea then is to iterate the pair of equations (28), (29) jointly in λ. Details of the skeleton expansion nature can be found in [3, 5, 6]. The main point to note is that while $\mathbf{g}^{-1}$, $\widetilde{\mu}$ in equations (28) and (29) are expanded in powers of λ, the function $\mathbf{g}$ is kept unexpanded as a basis term (or 'atom') of the skeleton expansion, temporarily ignoring its relationship as the inverse of $\mathbf{g}^{-1}$. The equal time value of the variable γ in equation (11) is taken from the exact sum-rule for $\mathcal{G}$ in equation (9). The initial values at $\lambda = 0$ are $\mathbf{g} = \mathbf{g}_0$ and $\widetilde{\mu} = \mathbb{1}$, and we must remember to use the product form equation (25) to determine the local Greens function γ in equation (11). We should note that when the source is turned off $\mathcal{V} \to 0$ we recover space and time translation invariance so that equation (25) is simply $\mathcal{G}(\vec{k},\ i\omega_j) = \mathbf{g}(\vec{k},\ i\omega_j).\widetilde{\mu}(\vec{k},\ i\omega_j)$, with the Matsubara frequency $\omega_j = (2j+1)\pi k_B T$. At low T, the leading singularities of $\mathcal{G}$ are co-located with those of $\mathbf{g}$, provided the caparison function $\widetilde{\mu}$ is sufficiently smooth- this situation is realized in all studies done so far.

2.3. The shift identities and second chemical potential u_0

Before proceeding with the iterative scheme, it is important to discuss a simple but crucial symmetry of the *t-J* model—*the shift invariance*, first noted in [10]. In an exact treatment shifting $t_{ij} \to t_{ij} + c_t\ \delta_{ij}$ with c_t arbitrary, is easily seen to be innocuous, it merely adds to equation (4) a term $-c_t\sum_\sigma \hat{N}_\sigma$ whereby the center of gravity of the band is displaced. (Here $\hat{N}_\sigma$ is the number operator for electrons with spin σ.) However in situations such as the λ expansion, the Gutzwiller constraint is released at intermediate values, here it has the effect of adding terms derivable from a local (i.e. Hubbard type) interaction term.[2] To see this consider the fundamental commutator term $[H_{tJ},\ X_i^{0\sigma_i}]$ in equation (13), here under the shift $t_{ij} \to t_{ij} + c_t\ \delta_{ij}$, the third term gives rise to an extra term $c_t X_i^{\bar{\sigma}_i\bar{\sigma}_i} X_i^{0\sigma_i}$. This term vanishes only in a Gutzwiller projected state, the EOM by themselves do not eliminate it. Its appearance is tantamount to adding a Hubbard like term $\frac{c_t}{2}\sum_i X_i^{\sigma\sigma} X_i^{\bar{\sigma}\bar{\sigma}}$ to the Hamiltonian H_{tJ}. As argued in [10] we would like the EOM for the Greens functions to be explicitly invariant under the above shift of t_{ij} to *each order in* λ. Enforcing this shift invariance to each order in the λ expansion plays an important 'watchdog' role on the λ expansion.

An efficient method to do so is to explicitly introduce an extra Lagrange multiplier u_0 through a term $\lambda u_0\sum_i N_{i\uparrow}N_{i\downarrow}$ to the Hamiltonian equation (4). This amounts to replacing $t_{ij} \to t_{ij} + \delta_{ij}\frac{u_0}{2}$ in all terms other than in the bare propagator $\mathbf{g}_0$. The u_0 term makes no difference when λ is set at unity in the exact series, since double occupancy is excluded. In practice, we set $\lambda = 1$ in equations that are truncated at various orders of λ, and the magnitude of u_0 is fixed through a second constraint. We thus have two variables to fix, namely u_0 and $\boldsymbol{\mu}$. We also have two constraints, the number sum-rules $n_\sigma = \mathbf{g}_{\sigma\sigma}(i\tau^-,\ i\tau)$, and $n_\sigma = \mathcal{G}_{\sigma\sigma}(i\tau^-,\ i\tau)$ (equation (9)). In the absence of a magnetic field the number densities n_σ reduce as $n_\sigma \to \frac{n}{2}$, where n is the number of particles per site.

After turning off the sources, in the momentum–frequency space we can further introducing two self energies $\Psi(k,\ i\omega_j)$, and $\Phi(k,\ i\omega_j)$ with

$$\widetilde{\mu}(\vec{k},\ i\omega_j) = 1 - \lambda\frac{n}{2} + \lambda\Psi(\vec{k},\ i\omega_j), \tag{30}$$

$$\mathbf{g}^{-1}(\vec{k},\ i\omega_j) = \mathbf{g}_0^{(-1)}(\vec{k},\ i\omega_j) + \lambda\left(\frac{n}{2}\varepsilon_k + \frac{n}{4}J_0\right) - \lambda\Phi(\vec{k},\ i\omega_j). \tag{31}$$

Here ε_k and J_k are the Fourier transforms of $-t_{ij}$ and J_{ij}. In the right hand side of equation (31), the second and third terms arise respectively from the equal-time limit of λY_1 and $\lambda\overrightarrow{X}.\mathbf{g}.\mathbf{g}^{-1}$ in equation (28) respectively. The two self energies $\Phi,\ \Psi$ are explicitly λ dependent, they vanish at infinite frequency for any λ. Thus we write

[2] Similarly we note that shifting $J_{ij} \to J_{ij} + c_J\delta_{ij}$ with arbitrary c_J also adds a similar unphysical local interaction term, as discussed in greater detail in [10].

$$\mathcal{G}(k,\, i\omega_j) = \mathbf{g}(k,\, i\omega_j) \times \widetilde{\mu}(k,\, i\omega_j). \tag{32}$$

The auxiliary Greens function satisfies a second sum-rule that is identical to equation (9), both may written in the Fourier domain:

$$(k_B T)\sum_{k,j} \mathrm{e}^{i\omega_j 0^+} G_{\sigma\sigma}(k,\, i\omega_j) = n_\sigma;\ \text{ for both } G = \mathcal{G} \text{ and } \mathbf{g}. \tag{33}$$

Equation (25) can now be written explicitly in the non-Dysonian form proposed in [3]

$$\mathcal{G}(\vec{k},\, i\omega_j) = \frac{1 - \lambda\frac{n}{2} + \lambda\Psi(\vec{k},\, i\omega_j)}{\mathbf{g}_0^{(-1)}(\vec{k},\, i\omega_j) + \lambda\frac{n}{2}\varepsilon_k + \lambda\frac{n}{4}J_0 - \lambda\Phi(\vec{k},\, i\omega_j)}. \tag{34}$$

We observe that simple FL-type self energies Ψ and Φ can, in the combination above, lead to highly asymmetric (in frequency) Dyson self energy $\Sigma(k,\, \omega)$ obtainable from the Greens function through $\Sigma = G_0^{-1} - G^{-1}$ [3, 5, 6, 10]. Finally we note that our calculations are performed in terms of spectral function obtainable from analytic continuation of the Matsubara frequencies into the upper complex half plane of frequencies:

$$\begin{aligned} \rho_{\mathcal{G}}(\vec{k},\, \omega) &= -\frac{1}{\pi}\, \Im m\, \mathcal{G}(\vec{k},\, i\omega_j \to \omega + i0^+), \\ \mathcal{G}(\vec{k},\, i\omega_j) &= \int \frac{\rho_{\mathcal{G}}(\vec{k},\, \omega)}{i\omega_j - \omega} \end{aligned} \tag{35}$$

and similarly defined spectral functions for variables $\mathbf{g}$, Φ, Ψ etc. Note that the physical spectral function $\rho_{\mathcal{G}}(\vec{k},\, \omega)$ is identical to $A(\vec{k},\, \omega)$, a notation used in much of experimental literature.

2.4. Summary of equations to second order in λ

In the following, we use the minimal second order equations [5–7] obtained by expanding equations (28) and (29) to second order in λ. The calculation is straightforward and a systematic derivation is detailed in [6], which is followed here. We use the abbreviation[3] $k \equiv (\vec{k},\, i\omega_n)$, and also redefine $\Phi(k) = \chi(k) + \varepsilon_k\Psi(k)$, keeping in mind that one set of terms in Φ have an external common factor of ε_k multiplied by all terms in Ψ. We next collect the answers below in terms of the two self energies χ, Ψ

$$\mathbf{g}^{-1}(k) = i\omega_n + \boldsymbol{\mu} - \underbrace{\varepsilon_k} + \lambda\frac{1}{4}nJ_0 - \varepsilon_k\left(-\lambda\frac{n}{2} + \lambda\Psi\right) - \lambda\chi(k), \tag{36}$$

the tag below the band energy $\underbrace{\varepsilon_k}$ can be ignored after the next paragraph. We now expand Ψ and χ from equations (28) and (29) in powers of λ. To the lowest two orders we find $\Psi = \lambda\Psi_{[1]} + O(\lambda^2)$ and $\chi = \chi_{[0]} + \lambda\chi_{[1]} + O(\lambda^2)$, where $\chi_{[0]} = -\sum_p \mathbf{g}_p\left(\varepsilon_p + \frac{1}{2}J_{k-p}\right)$.

The next step is to introduce u_0 explicitly: we write $\varepsilon_k \to \varepsilon'_k = \varepsilon_k - \frac{u_0}{2}$ in every occurrence of ε_k, except in the bare band energy term $\underbrace{\varepsilon_k}$ in equation (36).

$$\mathbf{g}^{-1}(k) = i\omega_n + \boldsymbol{\mu} + \lambda\frac{1}{4}nJ_0 - \frac{1}{2}u_0 - \widetilde{\mu}(k)\varepsilon'_k - \lambda\chi_{[0]}(k) - \lambda^2\chi_{[1]}(k). \tag{37}$$

Note that the shift with u_0 also applies to the term $\chi_{[0]}$, it now reads $\chi_{[0]} = -\sum_p \mathbf{g}_p(\varepsilon'_p + \frac{1}{2}J_{k-p})$. We note the expressions for $\chi_{[1]}$, $\Psi_{[1]}$ from [6] equations (65)–(67):

$$\chi_{[1]}(k) = -\sum_{pq}\left(\varepsilon'_p + \varepsilon'_q + \frac{1}{2}(J_{k-p} + J_{k-q})\right) \times (\varepsilon'_{p+q-k} + J_{q-k})\mathbf{g}(p)\mathbf{g}(q)\mathbf{g}(p+q-k), \tag{38}$$

$$\Psi_{[1]}(k) = -\sum_{pq}(\varepsilon'_p + \varepsilon'_q + J_{k-p})\mathbf{g}(p)\mathbf{g}(q)\mathbf{g}(p+q-k). \tag{39}$$

We now set $\lambda = 1$ and record the final equations:

$$\mathbf{g}^{-1}(k) = i\omega_n + \left(\boldsymbol{\mu} + \frac{1}{4}n(J_0 - u_0) - \frac{1}{2}u_0 + \sum_p \mathbf{g}_p\varepsilon_p + \frac{J_k}{2}\sum_p \mathbf{g}_p\cos p_x\right) - \widetilde{\mu}(k)\varepsilon'_k - \chi_{[1]}(k), \tag{40}$$

$$\widetilde{\mu}(k) = 1 - \frac{n}{2} + \Psi_{[1]}(k), \tag{41}$$

where we used a nearest neighbor J_{ij} and cubic symmetry in the simplifications. We can verify that the above expressions obey the shift invariance: if we shift $\varepsilon_k \to \varepsilon_k + c_0$, the arbitrary constant c_0 can be absorbed by shifting $\boldsymbol{\mu} \to \boldsymbol{\mu} + c_0$ and $u_0 \to u_0 + 2c_0$, and is thus immaterial. The band energy is given explicitly as

[3] We denote $k \equiv (\vec{k},\, i\omega_n)$, $\omega_n = (2n+1)\pi k_B T$ the Matsubara frequencies, N_s the number of sites and $\sum_k \equiv \frac{k_B T}{N_s}\sum_{k_x,k_y,\omega_n}$. J_k is the Fourier transform of the exchange.

$\varepsilon_k = -2t(\cos(k_x a_0) + \cos(k_y a_0)) - 4t' \cos(k_x a_0)\cos(k_y a_0)$, where t and t' are the first and second neighbor hopping amplitudes.

2.5. High energy cutoff scheme

The self consistent solution of the second order equations of equations (38)–(41) plus the number sum-rules, can be found numerically by discretizing the momentum and frequency variables on a suitable grid. This procedure can be carried out in a straightforward way for low $T \lesssim t$ and high hole densities $\delta \gtrsim 0.3$ (low particle densities $n \lesssim 0.7$). At lower hole densities or at high temperature $T \gg t$, the equations run into convergence problems. The origin of this problem is the formation of weak and featureless tails of the spectral functions extending to quite high energies. These tails are known to be artificial, since they do not occur in the exact numerical solutions where available. Thus the second order theory seems insufficient in the regime of low hole densities $\delta \lesssim 0.2$, where much of the current interest lies. A technically rigorous resolution of the problem of weak tails seems possible. However it requires the non-trivial calculation of higher order terms in the λ expansion. Such higher order terms oscillate in sign and hence cancellations at high energies are expected.

In view of the substantial magnitude of the program of summing the λ series to high orders, it seems worthwhile to investigate simpler and physically motivated approximations for improving the lowest order scheme. It turns out that there are a few interesting alternatives in this direction. In [5] we showed one convenient way to handle the high energy tail problem practically, through the introduction of a high energy cutoff. The choice of an objective cutoff was rationalized by considering two physically different limits, that of high particle density $n \to 1$ and the simpler high temperature limit, where related tails are found. The cutoff is chosen using the analytically available high T limit results and then applied to all densities and T.

The cutoff scheme of [5] is not rigorous, but enables us to extract meaningful results for low energy excitations from the second order λ equations, out to fairly low hole densities $\delta \lesssim 0.2$. It is benchmarked in the case of $d = \infty$, where the cutoff scheme quantitatively reproduces the spectral weights in the most interesting regime of low energies $|\omega| \ll t$, while erring somewhat at energies above the scale of quarter bandwidth. In [5, 7] the resulting physical quantities such as resistivity are shown to be in good correspondence to the exact results from DMFT. In view of this success we use a similar cutoff scheme for 2d below, with the expectation that the physics of the low energy excitations is captured. In the present 2d case we employ a single (re)-normalization the spectral function for each $\vec{k}$ as

$$\hat{\rho}_{\rm g}(\vec{k}, \omega) = \frac{1}{\mathcal{N}_k} W_T(\omega - \bar{\varepsilon}_k)\rho_{\rm g}(\vec{k}, \omega), \tag{42}$$

where W_T is a smooth window (even) function shown in figure 3 [5]. It is centered on $\bar{\varepsilon}_k$, the self-consistent location of the peak in $\rho_g(k, \omega)$, determined iteratively. It has width $4D$, where $2D$ is the bandwidth ($\sim 8t$ in this case). The constant $\mathcal{N}_k$ is fixed by the normalization condition $\int \hat{\rho}_{\rm g}(\vec{k}, \omega)\mathrm{d}\omega = 1$. In the present case of 2d we can impose this cutoff window at each $\vec{k}$ individually, so that only $\vec{k}$ states very far from the chemical potential are affected by the cutoff.

The two chemical potentials $\boldsymbol{\mu}$ and u_0 are determined through the number sum rules written in terms of the Fermi function $f(\omega) = (1 + \mathrm{e}^{\beta\omega})^{-1}$ and the spectral functions:

$$\sum_k \int \hat{\rho}_{\rm g}(k, \omega) f(\omega)\mathrm{d}\omega = \frac{n}{2} = \sum_k \int \rho_{\mathcal{G}}(k, \omega) f(\omega)\mathrm{d}\omega. \tag{43}$$

The set of equations equations (38)–(43) constitute the final set of equations to be computed. These are valid in any dimension, and reduce to the ones benchmarked in $d = \infty$ after setting $J \to 0$ [5, 7].

After analytically continuing $i\omega_n \to \omega + i0^+$ we determine the spectral function of the interacting electron spectral function $\rho_{\mathcal{G}}(\vec{k}, \omega) = -\frac{1}{\pi}\Im m\ \mathcal{G}(\vec{k}, \omega)$. The set of equations (1)–(5) was solved iteratively on $L \times L$ lattices with $L = 19, 37, 61$ and a frequency grid with $N_\omega = 2^{14}, 2^{16}$ points. We find that $L = 61$ produces the most accurate results at low temperature, while different L do not make a difference at high temperature. Also, $N_\omega = 2^{14}, 2^{16}$ lead to the same result in the relevant range of parameters. Therefore, we only display the result computed at $L = 61$ and $N_\omega = 2^{14}$ in this paper. Other details are essentially the same as in our recent study of the $d = \infty$, $J \to 0$ case in [5, 7].

3. Results

Band Parameters: The t-J model is studied on the square lattice with hopping parameters t and t' for first and second neighbors. The hopping parameter $t > 0$, while t' is varied between $-0.4t$ and $0.4t$, thereby changing

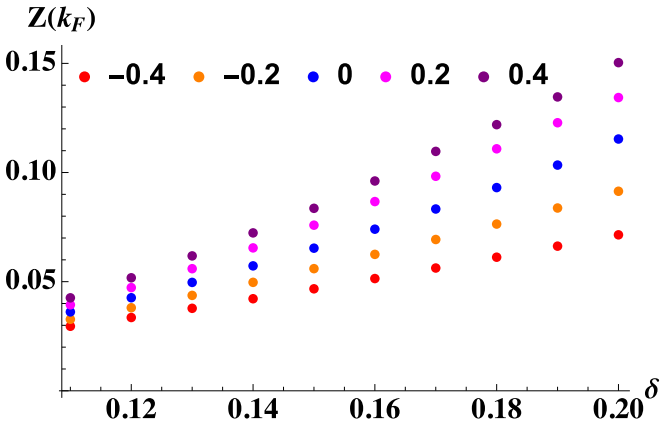

Figure 1. Hole density δ, and t'/t variation of the nodal $Z(k_F)$ at $T = 63$ K. The ratio t'/t is marked at the top. Decreasing t' has a similar effect to decreasing δ.

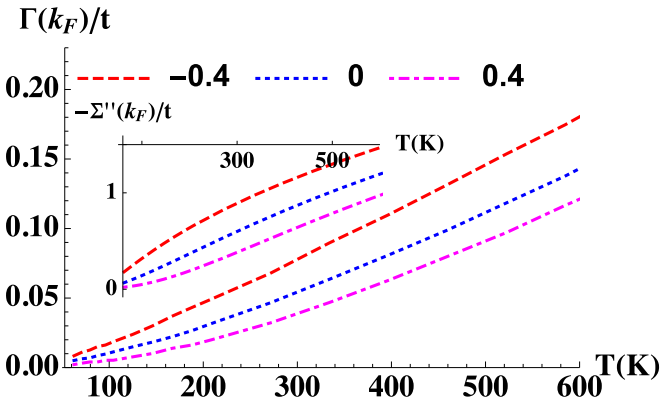

Figure 2. $\delta = 0.15$: the decay rate equation (44) and (inset) the nodal $-\Im m\ \Sigma(k_F)$. The ratio t'/t is marked at top. While $t' = 0.4t$ has a positive curvature for both variables, $t' = -0.4t$ displays a prominent negative curvature in $-\Im m\Sigma$, and an almost flat Γ.

the Fermi surface (FS) from hole-like to electron-like. Parameters relevant to cuprate High T_c materials are summarized in [2, 11] [4]. Following [2] we assume $t \sim 0.45$ eV, giving a bandwidth ~3.6 eV.

Single-particle spectrum: The quasiparticle energy $E(\vec{k})$ and quasiparticle weight $Z(\vec{k})$ are found from $\mathcal{G}$ as usual [5]. In figure 1 we display the hole density δ and t' dependence of the low temperature $Z(k_F)$, along the nodal (i.e. $\langle 11 \rangle$) direction. The typical magnitudes of Z are comparable or lower than those reported in $d = \infty$ [5]. A *new and important feature* is the strong sensitivity of $Z(k_F)$ to the sign and magnitude of t'/t. Both decreasing t' (at fixed δ) and decreasing δ (at fixed t') reduce Z. This feature is basic to understanding our main results. We next study the decay rate of the electrons

$$\Gamma(\vec{k}) = -Z(\vec{k}) \times \Im m\ \Sigma(\vec{k}, E(\vec{k})), \tag{44}$$

found as the half-width at half-maximum of the spectral function $\rho_{\mathcal{G}}(\vec{k}, \omega)$ at fixed $\vec{k}$. We display the T variation of Γ and $-\Im m\ \Sigma$ at the Fermi surface for three representative values of t'/t in figure 2. Both variables display considerable variation with modest change of T. The case of $t' > 0$ shows a distinct quadratic T dependence, but for $t' \leqslant 0$ we note the strong reduction, or absence, of such a quadratic dependence. Below we note a closely parallel T and t' dependence of the resistivity.

In figure 3 we display the photoemission accessible peak heights of the spectral function $\{t \star \rho_{\mathcal{G}}(\vec{k}, \omega)\}_{\max}$ over the BZ at three representative values of t'/t, at three temperatures $T = 63,\ 210,\ 334$ K.The peaks locate the interacting Fermi surface and its thermal sensitivity. The Fermi surface closely tracks the non-interacting FS, changing from hole-like in panels (a)–(c) to strongly electron-like in panels (g)–(i). This implies that the momentum dependence of the Dyson self energy is mild. In contrast a strong momentum dependence would distort the Fermi surface shape significantly—while retaining the Luttinger–Ward volume. Several features are

[4] In high T_c systems [2] estimate $t' \lesssim -.27$ for BSCCO, while for LSCO $t' \sim -0.16t$. NCCO is modeled with $t' > 0$ after invoking a particle hole transformation. In this case we must flip the sign of the calculated R_H and Θ_H to compare with data.

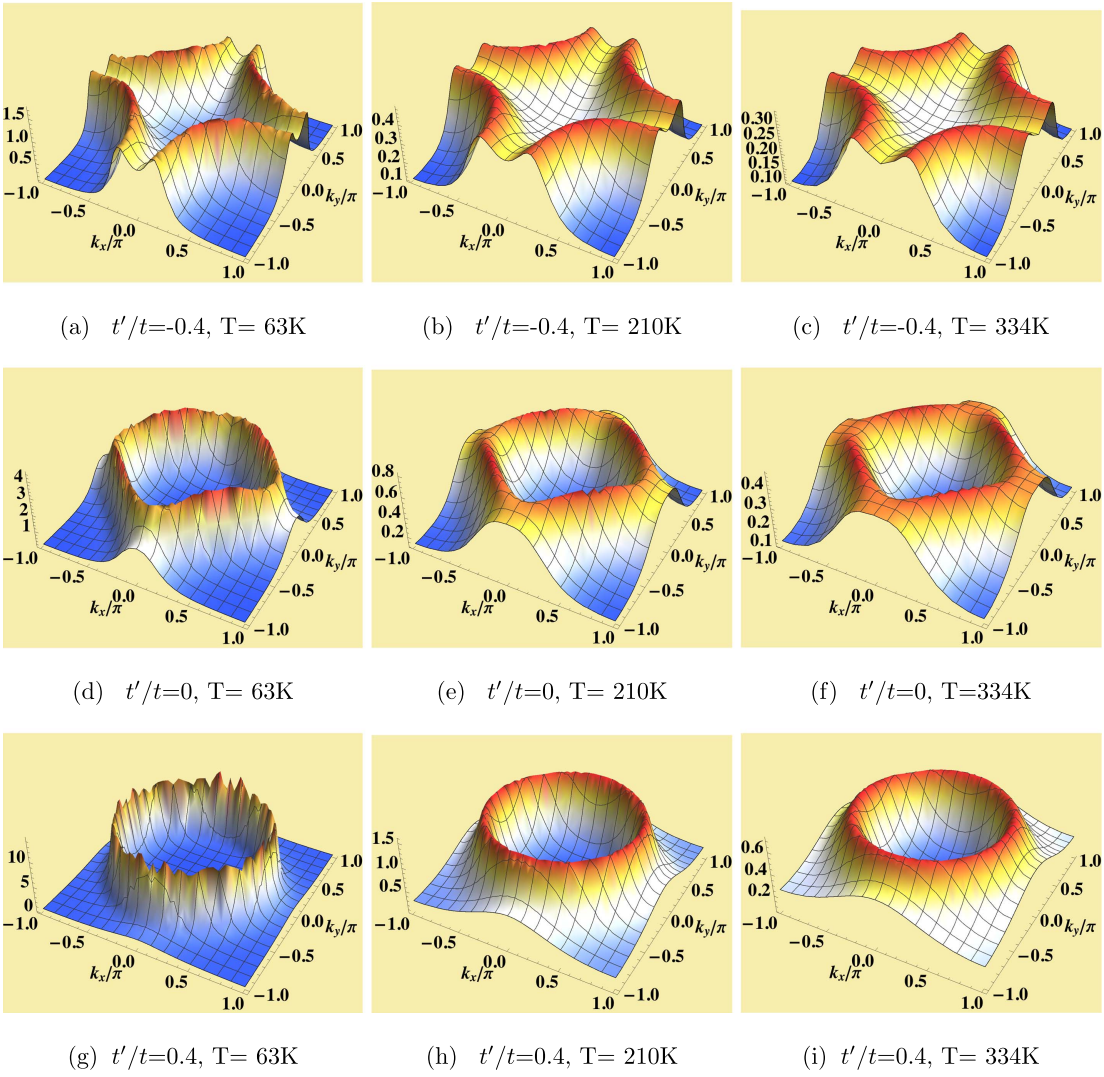

Figure 3. The spectral function $A(\vec{k}, \omega)$ peak heights over the zone at a fixed hole density $\delta = 0.15$, t' increasing from top to bottom and T increasing from left to right. At a fixed T, the peak heights increase on proceeding down any column (i.e. increasing t'/t), signifying sharper quasiparticles. Proceeding across any row (i.e. increasing T) illustrates the dramatic thermal sensitivity in all cases. Recalling that our bandwidth is ~3.6 eV, we observe that upon warming from 63K to 210K, a tiny variation (~0.35%) of temperature relative to the bandwidth, the peak height drops by a factor between *5* and *10*, followed by a more gentle fall to 334K. This extraordinary thermal sensitivity is characteristic of our solution of the t-J model, it is also reflected in other variables discussed here, such as the resistivity.

noteworthy. The peaks are higher in the nodal relative to the anti-nodal direction at low T. We observe the high sensitivity to warming, in going from $T = 63$ K to $T = 334$ K a small (~0.7%) change in T relative to the bandwidth causes a five to fifteen-fold drop in the spectral peaks at the Fermi surface. This is correlated to the thermal variation of $-\Im m\ \Sigma$ at the same set of t', shown in the inset of figure 2, since the intensity at k_F is essentially the inverse of this object. Meanwhile the background spectral weight rises rapidly in all cases, to a roughly similar magnitude. The figure shows that at low T the curve with $t' > 0$ has much higher peaks than $t' \leqslant 0$, giving the impression of weaker correlations. However the drop on warming is the largest in this case, which signifies another facet of strong correlations. The heights of the spectral peak and that of the background is predicted quantitatively in figure 3. Their ratio is straightforward to measure in angle resolved photo emission studies, and we suggest it should be interesting to closely study this ratio experimentally, as a check of the theoretical understanding of the temperature dependence of $\Im m\Sigma(k_F)$ and the decay rate $\Gamma(k_F)$.

Resistivity: We now study the behavior of the resistivity from electron–electron scattering. We use the popular bubble approximation, factoring the current correlator as $\langle J(t)J(0)\rangle \sim \sum_k v_k^2 \mathcal{G}^2(k)$, where the bare current vertex is the velocity $\hbar v_k^\alpha = \frac{\partial \varepsilon_k}{\partial k_\alpha}$. In tight binding theory v_k^α oscillates in sign, resulting in a vanishing average over the Brillouin zone. This oscillation is expected to reduce magnitude of the vertex corrections [12]. For a 3d metal having well separated sheets in the c direction (c_0 the separation of the sheets), with each sheet represented by the 2d *t-J* model, the DC resistivity ρ_{xx} can be written in terms of the electron spectral function as follows. We define a dimensionless resistivity $\bar{\rho}_{xx}$ whose inverse is given by

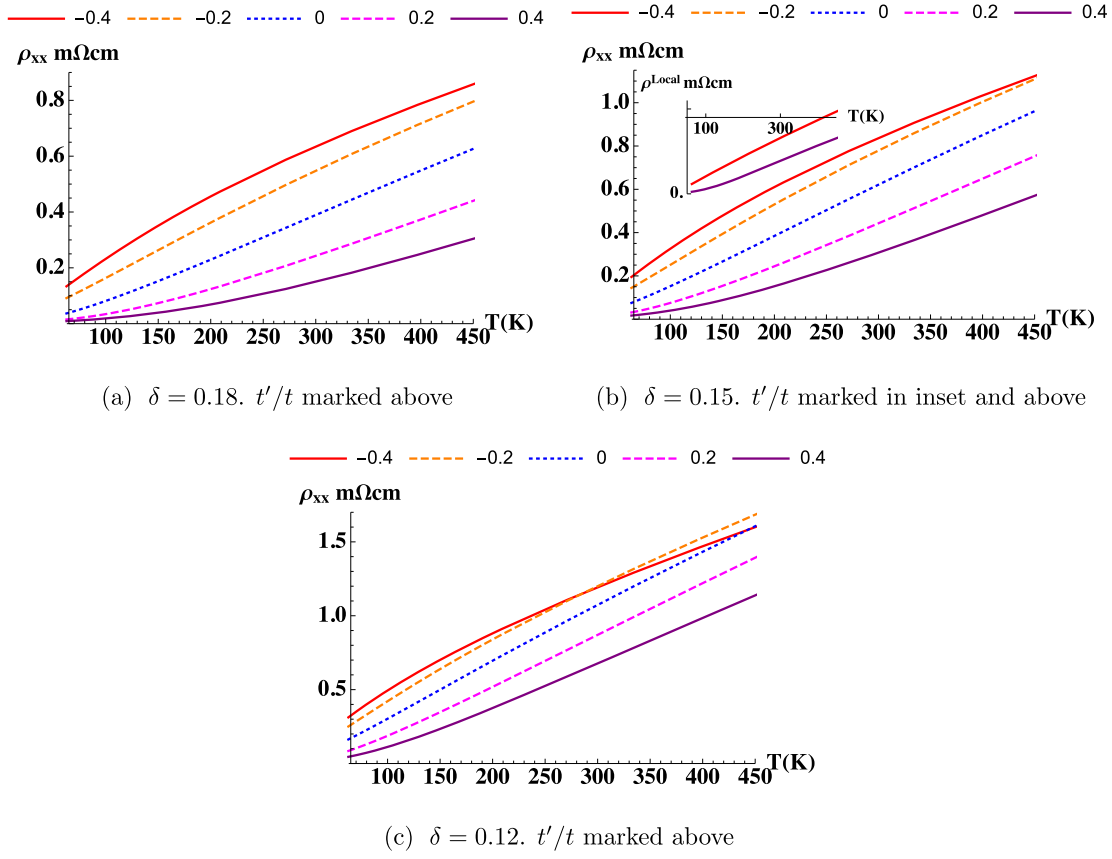

Figure 4. The resistivity at three typical densities. The lowest T region is expected to be cutoff by superconductivity. For a fixed T the curvature changes from positive (concave) to negative (convex) as t'/t varies upwards in each panel, and also slightly as δ increases across the panels—resembling the experimental findings of [15–19]. The Fermi liquid $\rho \propto T^2$ regime is suppressed as t' becomes more negative, and is difficult to discern here with $t'/t = -.4$. Panel (b) (inset) is the local approximation from equation (48). It illustrates the t' dependence of $\rho^{\rm Local}$ from the spectral functions, or equivalently the self energies. The t' dependence of the velocities, included in the result from equation (45) in the main panel (b), exhibits an enhanced convexity of the resistance. The magnitude of ρ_{xx} increases with decreasing δ within the displayed range of T. The electron-doped case $t' > 0$ shows a somewhat smaller resistivity than the hole-doped case $t' \leqslant 0$. In the latter, ρ_{xx} approaches the unitarity value 1.71 mΩcm only at the lowest δ and highest T.

$$\bar{\sigma}_{xx} = \langle \Upsilon(\vec{k})(\hbar v_k^x)^2/a_0^2\rangle_k, \tag{45}$$

where $\langle A\rangle_k \equiv \frac{1}{N_s}\sum_{\vec{k}} A(\vec{k})$, while the momentum resolved relaxation scale is:

$$\Upsilon(\vec{k}) = (2\pi)^2 \int_{-\infty}^{\infty} {\rm d}\omega\ (-\partial f/\partial\omega)\rho_{\rm G}^2(\vec{k},\omega), \tag{46}$$

and $f \equiv 1/(1+\exp\beta\omega)$ is the Fermi function. This object resembles the spectral peaks in figure 3, losing height and broadening rapidly with T. The physical 3d resistivity is given by $\rho_{xx} = \rho_0 \times \bar{\rho}_{xx}$, where $\rho_0 \equiv c_0 h/e^2$ (~1.71 mΩ cm) serves as the scale of resistivity[5], and using the measured values of the lattice constants we can express our results in absolute units. For understanding the magnitude of the inelastic scattering it can be useful to convert the resistivity into the dimensionless parameter $\langle k_F\rangle \lambda_m$ of an effective 2d continuum theory, where λ_m is the mean-free-path and where $\langle k_F\rangle$ is an (angle averaged) effective Fermi momentum. We can use a relation argued for in [6][13, 14]

$$\langle k_F\rangle\ \lambda_m = \frac{hc_0}{e^2\rho_{xx}} = \frac{1}{\bar{\rho}_{xx}}. \tag{47}$$

In [13, 14] (see footnote 6) the authors note that in a metallic system this parameter is expected to be greater than unity, and its least value is $\langle k_F\rangle\ \lambda_m = 1$ for the case of unitary (impurity) scattering. Thus we expect that $\rho_{xx} \leqslant \rho_0$, i.e. $\bar{\rho}_{xx} \leqslant 1$ in a good metal. The Ioffe–Regel–Mott resistivity scale used in [5, 7, 8] provides a similar measure for quantifying the magnitudes of the resistivity found in strongly correlated metals. However we should keep in mind that both estimates suffer from ambiguities in defining a precise threshold value of resistivity, since factors of 2 (or of 2π) cannot be ruled out in equation (47).

[5] The numerics assume a bct unit cell (a, a, c) with $a = 3.79\ \mathcal{A}^0$ and $c = 13.29\ \mathcal{A}^0$. In the expression for ρ_0, c_0 corresponds to the interlayer separation $c_0 = c/2$. In equations (50) and (51) we use $v_0/|e| = .596 \times 10^{-3}$ cm^3 C^{-1} and $\Phi_0/\Phi = 1440$ with $B = 10$ T.

[6] See equation (6) in [13]. The origin of this formulais simple to understand, 3d conductivity is written in terms of the two dimensional density as $\sigma = \frac{n_{2d}e^2\tau}{c_0 m}$, and writing $n_{2d} = k_F/(2\pi)$ and $\lambda_m = \tau\hbar k_F/m$ we obtain $\sigma = e^2/(hc_0)k_F\lambda_m$.

Figure 4 shows the temperature dependence of the resistance at three densities, and their strong variation with t'/t. J is taken as 900 K here, varying J between 0 and 1500 K makes almost no difference at these temperatures. We see that the scale of the resistivity for $t' \leqslant 0$ exceeds the (approximately estimated) unitarity value 1.71 mΩ cm for the lowest δ and the highest displayed T. On the other hand $t' > 0$ shows a considerably smaller resistivity at most densities.

In all curves we see that the curvature changes from positive (for $t' \geqslant 0$) to negative (for $t' < 0$) at say 150 K. To understand the role of t'/t we note that the resistivity in equation (45) depends on t'/t through the velocity v_k^x, in addition to a dependence through the self energies equations (38), (39). To gauge their relative importance it is useful to examine a local approximation of equation (45) where the two functions are averaged separately over momentum:

$$\bar{\sigma}_{xx}^{\text{local}} = \langle \Upsilon(\vec{k}) \rangle_k \times \langle (\hbar v_k^x)^2 / a_0^2 \rangle_k. \tag{48}$$

The velocity squared average is independent of the sign of t', therefore the local approximation, shown in figure 4, inset of panel (b), probes only the dependence through equations (38), (39). Comparing the inset and main figure in panel (b), we see that at $t' = 0.4t$ both resistivity curves display a positive curvature. At $t' = -0.4t$ we see that ρ^{Local} is essentially linear in T, while ρ_{xx} shows a negative curvature. The difference is therefore related to the velocity factors, which are very different effect between $t' < 0$ and $t' > 0$. These cause the integrals to have very different thermal variation.

Hall response: Within the bubble scheme, we may also calculate the Hall conductivity [9, 20, 21] as $\sigma_{xy} = -2\pi^2 / \rho_0 \times \left(\frac{\Phi}{\Phi_0}\right) \times \bar{\sigma}_{xy}$, the dimensionless conductivity:

$$\bar{\sigma}_{xy} = \frac{4\pi^2}{3} \int_{-\infty}^{\infty} \mathrm{d}\omega \, (-\partial f/\partial \omega) \langle \rho_{\text{G}}^3(k, \omega) \eta(k) \rangle_k \tag{49}$$

and $\eta(k) = \frac{\hbar^2}{a_0^4} \left\{ (v_k^x)^2 \frac{\partial^2 \varepsilon_k}{\partial k_y^2} - (v_k^x v_k^y) \frac{\partial^2 \varepsilon_k}{\partial k_x \partial k_y} \right\}$. Here $\Phi = B a_0^2$ is the flux (see footnote 5) and $\Phi_0 = hc/(2|e|)$ is the flux quantum. In terms of these we can compute the Hall constant R_{H} and Hall angle Θ_{H} from

$$c\, R_{\text{H}} = -\frac{4\pi^2 v_0}{|e|} \, \bar{\sigma}_{xy} \times \bar{\rho}_{xx}^2, \tag{50}$$

$$\cot(\Theta_{\text{H}}) = -\frac{1}{2\pi^2} \frac{\bar{\sigma}_{xx}}{\bar{\sigma}_{xy}} \times \frac{\Phi_0}{\Phi}, \tag{51}$$

with $v_0 = (a_0^2 c_0)$ (see footnote 5). We also define the Hall number as

$$n_{\text{H}} = -\frac{v_0}{|e| c R_{\text{H}}} = \frac{1}{4\pi^2} \frac{\bar{\sigma}_{xx}^2}{\bar{\sigma}_{xy}}, \tag{52}$$

where the definition ensures that in the limit of a circular Fermi surface without interactions, $n_{\text{H}} \to n$, where n is the number of *electrons* per copper in the effective single band t-J model (see footnote 8). The tight binding Fermi surface in the presence of t' is not circular, but rather resembles the surfaces shown in figure 3. Under these conditions we can evaluate the conductivities in equations (45) and (49), using an approximate Lorentzian spectral function peaked at the bare Fermi surface[7]: The resulting 'bare' Hall number n_{H}^0 contains the corrections due to the curvature of the Fermi surface, including the change in sign in going from open to close surfaces as t' becomes negative. It is therefore helpful to compare our computed Hall number n_{H}, containing the effects of interactions and a complicated scattering rate Γ, with n_{H}^0 containing only the band effects. This helps us to gauge the effects of interactions, left out in the formula for n_{H}^0. The computed n_{H}, bare Hall number n_{H}^0 and their ratio $n_{\text{H}}/n_{\text{H}}^0$ are shown in table 1. We see that strong correlation generally suppresses n_{H} from the bare value n_{H}^0, in some cases by as much as 40%. The n_{H}^0 itself differs from n quite substantially, depending on doping, temperature and t', and therefore one must exercise great care in extracting carrier densities from Hall numbers.

In figure 5 we display the computed Hall variables. In panel (a) $\tan \Theta_{\text{H}}$ is shown for two values of t'/t displaying hole-like and electron-like behavior. A decrease in hole density reduces the magnitude in either case. In panel (b) we display the computed $\cot(\Theta_{\text{H}})$ versus T^2 with three values of t' giving an electron-like FS. We note that $\cot \Theta_{\text{H}}$ is approximately linear with T^2 [22–24] and is strongly affected by the magnitude of t'. The two distinct $\cot(\Theta_{\text{H}}) \propto T^2$ regimes seen in figure 5(b) are also seen in many experiments but seem to have evaded attention so far. In [24] it is noted that the bending temperature corresponds to a crossover from the Fermi liquid

[7] These definitions lead to intuitive results in simple cases. For 2-d electrons with $\varepsilon_k = \hbar^2 k^2/(2m)$, and a Lorentzian $\rho_{\text{G}}(k, \omega) = \frac{1}{\pi} \frac{\Gamma_0}{\Gamma_0^2 + (\omega + \varepsilon_F - \varepsilon_k)^2}$, upon setting the width $\Gamma_0 \to 0$, we recover the Drude result $\sigma_{xx} = n q_e^2 \tau/m$ and $\bar{\sigma}_{xy} = n \left(\frac{\hbar^2}{2m a_0^2 \Gamma_0}\right)^2$ with $\tau = \hbar/(2\Gamma_0)$. Thus $|e| R_H c/v_0 = -1/n$ in equation (50), and $\cot(\Theta_H) = -1/(\omega_c \tau)$ in equation (51) where $\omega_c \equiv |e|B/(mc)$. If on the other hand we take ε_k from the Fourier transform of $-t_{ij}$, the limit $\Gamma_0 \to 0$ yields the "bare" Hall number n_H^0, incorporating the effects of a non-circular band structure.

Table 1. The Hall number $n_{\rm H}$ from equation (52), the bare Hall number $n^0_{\rm H}$, and their ratio $n_{\rm H}/n^0_{\rm H}$. $n_{\rm H}$ is computed at lattice size 61 $\times$ 61 at $T = 63$ K and $n^0_{\rm H0}$ is computed in the bare band with lattice size 4000 $\times$ 4000 at $T = 0$. Note that the ratio $n_{\rm H}/n^0_{\rm H}$ varies from .6 to .8. This substantial correction is due to strong correlations. Therefore the inverse problem of deducing the carrier density n from the Hall number $n_{\rm H}$ is quite complex. Finite temperature effects make this even more complicated, as seen in figure 5.

Electron density	Hall number	$t' = -0.4$	$t' = -0.2$	$t' = 0$	$t' = 0.2$	$t' = 0.4$
	$n_{\rm H}$	−0.819	−2.514	1.119	0.679	0.675
$n = 0.82$	$n^0_{\rm H}$	−1.163	−3.389	1.51	0.879	0.823
	$n_{\rm H}/n^0_{\rm H}$	0.704	0.742	0.741	0.773	0.82
	$n_{\rm H}$	−.768	−1.918	1.249	0.67	0.65
$n = 0.85$	$n^0_{\rm H}$	−1.137	−2.448	1.774	0.927	0.855
	$n_{\rm H}/n^0_{\rm H}$	0.676	0.783	0.704	0.722	0.76
	$n_{\rm H}$	−.706	−1.479	1.436	0.67	0.637
$n = 0.88$	$n^0_{\rm H}$	−1.109	−1.963	2.148	0.977	0.884
	$n_{\rm H}/n^0_{\rm H}$	0.637	0.754	0.669	0.686	0.721

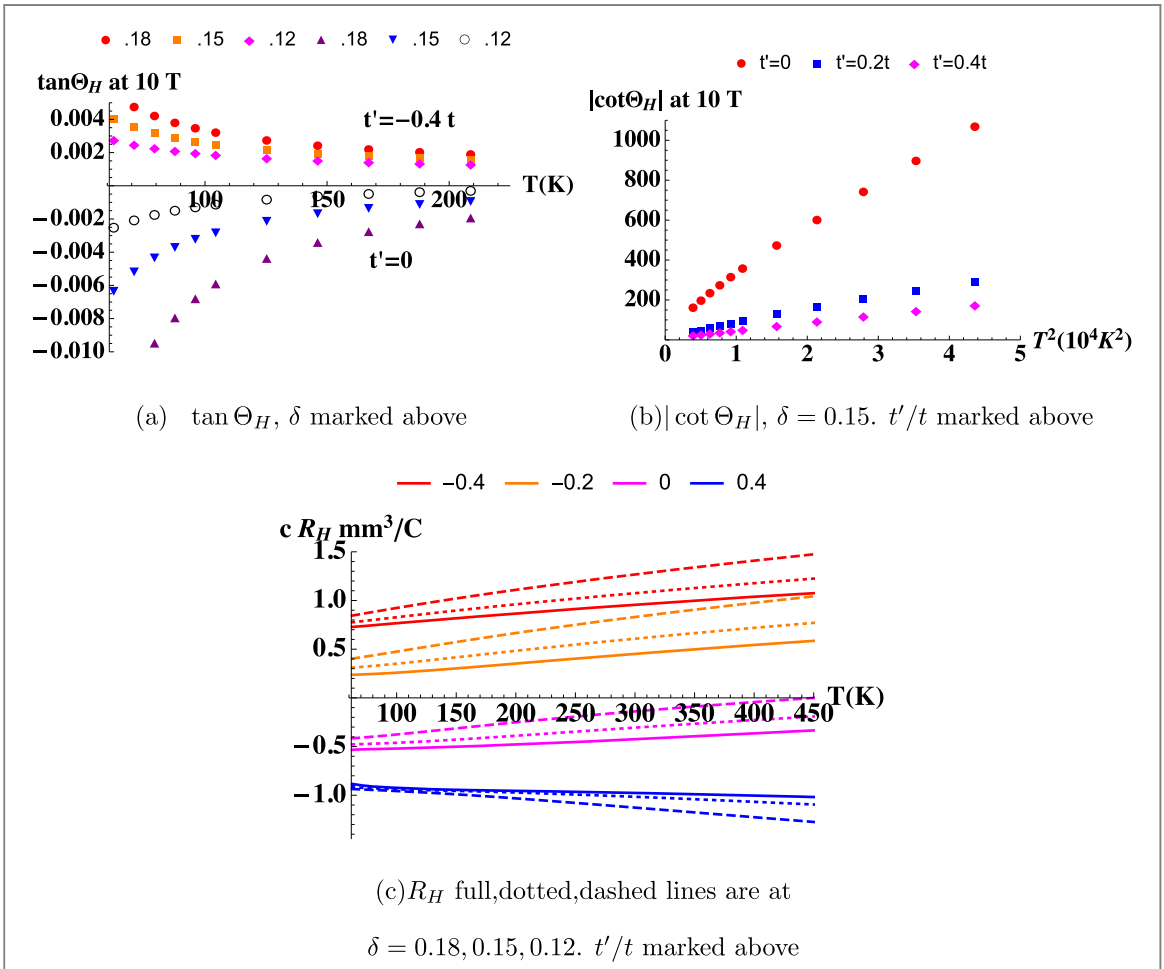

(a) $\tan\Theta_H$, δ marked above

(b) $|\cot\Theta_H|$, $\delta = 0.15$. t'/t marked above

(c) R_H full,dotted,dashed lines are at $\delta = 0.18, 0.15, 0.12$. t'/t marked above

Figure 5. Panel (a) $\tan\Theta_{\rm H}$ for $B = 10$ T at three densities versus T. The set with $t' = -0.4t$ have a hole-like FS while the set with $t' = 0$ an electron-like FS. In both cases we see a rapid fall-off with T, and a decreasing magnitude with δ. Panel (b) for $B = 10$ T at $\delta = 0.15$ shows $|\cot(\Theta_{\rm H})|$ for three values of t'/t. It is approximately linear with T^2 over the range. In fact it is linear on both sides of a bend, which is also seen in data [17, 19, 22–27] but seems to have evaded comment in literature. Panel (c) gives the T dependent $R_{\rm H}$ for three densities, each with four values of t'/t. The magnitude of $cR_{\rm H}$ at lowest T is related to the Hall numbers $n_{\rm H}$ in table 1 via the relation equation (52) $cR_{\rm H} = -v_0/n_{\rm H}|e|$, where $v_0/|e| = .596$ mm^3 C^{-1}. The sign change resembles the change seen in experiments [28].

to a strange metal, and is therefore of fundamental importance. In panel (c) we show the Hall constant $R_{\rm H}$ at three densities for representative values of t'/t. Its sign is electron-like for $t' > 0$ and hole-like for $t' \leqslant 0$, tracking the change in topology of the Fermi surface in figure 2. The magnitude of $R_{\rm H}$ is substantially affected by changing t'. This is a strong correlation effect, and discourages envisaging any simple relationship between the Hall number and hole density.

4. Discussion

Using the recently developed second order equations of the ECFL theory in [5], we have presented results for the 2d *t-J* model at low and intermediate temperatures. In keeping with our recent findings for the $d = \infty$ solution of *the same equations*, we note that the quasiparticle weight $Z(k_F)$ is non-zero, but remarkably small. This *fragile* FL therefore has an extremely low effective Fermi temperature, above which it displays characteristics of a Gutzwiller correlated strange metal, as listed in [5, 7], including a resistivity that is linear in T.

By varying t', the second neighbor hopping at a fixed t and J, we found in figure 1 a remarkable variation of the quasiparticle weight $Z(k_F)$ that is characteristic of the 2d square lattice, with no simple analog in $d = \infty$. We found $t' < 0$ leads to a considerable reduction in its magnitude, while $t' > 0$ leads to a larger value and thus a more robust FL. A direct calculation of the single particle spectral width $\Gamma = -Z\Sigma''$ confirms this observation in figure 2, and when studied as a function of the temperature, shows a much larger magnitude, and hence broader spectral lines.

In figure 3 we present the Fermi surface, as found from the peaks of the spectral function. The shapes of the Fermi surfaces are quite close to those implied by the bare band parameters. This implies that the momentum dependence of the self energy, while non-zero, is fairly small. This also suggests that the vertex corrections, neglected here in 2d, may actually be quite small as well. Two key results concern the spectral heights over the Brillouin zone, and the resistivity as a function of T at various densities and t'. The spectral height is the peak value of $\rho_{\mathcal{G}}(\vec{k}, \omega)$ scanned over ω, and equals the inverse of the least magnitude of $\Im m\Sigma(\vec{k}, \omega)$. In figure 3 we present both the T evolution (going horizontally) and the t' evolution (going vertically) of this important object visible in ARPES. We note that $t' < 0$ model with a very small Γ also displays a rapid loss of coherence on warming. The quasiparticle peaks drop rapidly, while the valleys, representing the background spectral weight in photoemission, catch up with the peaks in magnitude. A similar variation happens for $t' = 0$ but the drop of the peak heights is more pronounced. The case of $t' > 0$ has the largest drop of peak heights, while its effective Fermi temperature is the largest of the three cases. It follows that the electron doped case has a more robust FL appearance for T lower than its Fermi scale. Our study provides absolute scale values for these observable heights, and it should be interesting to study these experimentally for comparison. Towards that objective we note that $t' > 0$ maps to the electron doped High T_c superconductors, while $t' \leqslant 0$ maps to the hole doped cases, as we may also deduce from the shapes of the Fermi surfaces in the above figure.

The other key result concerns the resistivity. We are able to calculate the longitudinal resistivity ρ_{xx} on a *doubly absolute scale*, both the magnitude of ρ_{xx} and that of T are given in physical units by using reasonable values for the basic parameters of the *t-J* model and the lattice constants figure 4. We find essentially the experimentally observed scales for both axes, and there is room for further adjustments of bare scales if needed. The main finding is that as δ is varied towards half filling, the regime of linear resistivity increases in the hole-like cases ($t' \leqslant 0$) and the quadratic dependence regime shrinks to very low T scales, falling below the known superconducting transition temperatures. The other important finding is that the concavity (convexity) of resistance versus T, usually taken to denote a (non) FL behavior, requires an enlarged viewpoint; we find that the sign of t' flips the two cases. As an example, the case $t' \leqslant 0$ has a pronounced convex regime at low T. This could be naively ascribed to a non-FL behavior, but in reality is a crossover range to the strange metal regime.

We also present results in figure 5 for the Hall constant and the Hall angle. These are calculated using simple versions of the Kubo formula, found by neglecting the vertex corrections, in the same spirit as the longitudinal resistivity. This approximation is as yet untested against exact results and hence requires some caution. We find that the Hall angle changes sign with t'. The $\cot(\Theta_{\rm H})$ is found to be roughly linear with T^2, in agreement with the experimental situation. As noted above, the $\cot(\Theta_H) \propto T^2$ regime is followed at higher T by a bend (or kink) corresponding to a crossover from the Fermi liquid to a strange metal, and is therefore important. A similar bend is also seen in many experiments [17, 19, 22–27], but seems to have evaded comment so far. In [24] this kink is discussed further and its connection to the crossover is explained.

In table 1, we present the Hall number n_H obtained from the Hall constant for various n and t'/t. It is compared with the corresponding n_H^0 obtained from a non-interacting theory that incorporates the band-structure effects of changing curvature when $t' < 0$. We note that the n_H^0 already captures the changes in sign due to varying t'. However, there are substantial quantitative corrections even at the lowest T, originating in strong correlations. This makes the inference of electron density n from n_H quite non-trivial; table 1 provides an estimate of the errors involved in this inversion.

5. Conclusions

In this work, we employed a recently developed scheme from the ECFL theory where the second order λ expansion terms are supplemented with a high energy cutoff. This scheme has been benchmarked in $d = \infty$

against DMFT [5, 7] for computing transport and other low energy excitations, giving good agreement with exact numerical results. As detailed in [5] the magnitude of the quasiparticle weight Z is somewhat lower in this scheme as compared to the exact DMFT values for hole density $\delta \lesssim 0.8$. In this work *the same equations* are applied to the 2-d tJ model. While the close agreement found in the $d = \infty$ case might not guarantee the accuracy of these results in $d = 2$, it is plausible that the variations of resistivity and Hall constant, induced by the magnitude and sign of t' found here, will persist in more exact (future) results. Hence it seems that we can draw some useful conclusions already, especially with regard to the difference between hole and electron doping.

We have shown a range of results for the 2d *t-J* model, obtained by varying different parameters within our scheme. It is interesting that the magnitudes of various transport variables, presented here in physical units[8], are roughly on the scale of reported measurements [15, 25, 16–19, 26, 27]. Although it is not our primary aim here to produce exact fits, we note that the agreement can be improved in many cases with suitable changes of the bare (band) parameters.

In the range of parameters considered here, a metallic state has been posited, and therefore the role of the exchange J is limited; we find very little variation of the transport quantities with a change in J. The transport parameter variation with density seems very similar to that found in $d = \infty$ in [5, 7, 8] where a large variety of Gutzwiller correlated metallic states were shown to arise [7], with their origin in the $U = \infty$ or Gutzwiller correlation rather than with J. The added feature in $d = 2$ is the important role played by t', as stressed here. We expect magnetic, superconducting and possibly other broken symmetry states at the lowest T and δ to arise, largely due to the effect of J. Further work is necessary to find reliable calculational schemes for these broken symmetry states.

A few broad conclusions suggest themselves. The parameter t'/t plays a key role in determining the low-energy scales. In figure 1 we see that the quasiparticle weight Z has a large variation with t'. The origin of this sensitivity lies in the self energies in equations (39), (38), where combinations of the band energies ε_k play the role of an effective interaction. Varying t'/t therefore changes the self-energies strongly, in contrast to the usual weak change via the band parameters in equation (37).

Our main findings are as follows. (I) The spectral functions are highly sensitive to thermal variation; in figure 3 we observe a five to fifteen fold drop in intensity with a variation of k_BT about 1/100th the bandwidth ∼3.6 eV. This is in severe conflict with expectations from conventional theories of metals. (II) We note from figure 4 that with $t' \leqslant 0$, a FL resistivity $\rho \propto T^2$ is seen only at very low T. The very low T (FL) regime is followed by a 'strange metal' regime, also at low T, where we find a ρ versus T curve, with zero or negative curvature. This regime parallels the Gutzwiller-correlated strange metal regime reported in $d = \infty$ [7], the negative curvature making it even stranger. (III) For the electron-doped case $t' > 0$, figure 4 shows that the curvature is positive and the FL regime extends to higher temperatures.

It is significant that the ECFL theory captures the diametrically opposite resistivity behaviors of hole doped [15–17] and electron doped materials [18, 19] within the same scheme, only differing in the sign of t'/t. The resistivity curvature mapping of [15] can also be viewed in terms of a variation of this ratio and the temperature, as in figure 4. In conclusion this work provides a sharp picture of the difference made by the second neighbor hopping t' in the presence of Gutzwiller correlations. It also yields quantitative results for several famously hard to compute variables in correlated matter, that are in rough agreement with a variety of experiments.

Acknowledgments

We thank Edward Perepelitsky and Sergey Syzranov for helpful comments on the manuscript. The work at UCSC was supported by the US Department of Energy (DOE), Office of Science (BES) under Award # DE-FG02-06ER46319. Computations reported here used the XSEDE Environment [29] (TG-DMR160144) supported by National Science Foundation grant number ACI-1053575.

References

[1] Anderson P W 1987 *Science* **235** 1196
[2] Ogata M and Fukuyama H 2008 *Rep. Prog. Phys.* **71** 036501
[3] Shastry B S 2011 *Phys. Rev. Lett.* **107** 056403
[4] Shastry B S 2014 *Ann. Phys.* **343** 164–99
Shastry B S 2016 *Ann. Phys.* **373** 717–8 (erratum)
[5] Shastry B S and Perepelitsky E 2016 *Phys. Rev.* B **94** 045138
Žitko R, Hansen D, Perepelitsky E, Mravlje J, Georges A and Shastry B S 2013 *Phys. Rev.* B **88** 235132
Shastry B S, Perepelitsky E and Hewson A C 2013 *Phys. Rev.* B **88** 205108

[8] From [5, 7] we may infer that the Z in the present calculation is a bit too low for $t' = 0$ and $.12 \leqslant \delta \leqslant .15$. This is expected to result in overestimating ρ_{xx} by a factor ∼3 at $T = 450$ K.

[6] Perepelitsky E and Shastry B S 2015 *Ann. Phys.* **357** 1
[7] Ding W, Žitko R, Mai P, Perepelitsky E and Shastry B S 2017 arXiv:1703.02206v2
[8] Deng X Y, Mravlje J, Žitko R, Ferrero M, Kotliar G and Georges A 2013 *Phys. Rev. Lett.* **110** 086401
[9] Xu W, Haule K and Kotliar G 2013 *Phys. Rev. Lett.* **111** 036401
[10] Shastry B S 2013 *Phys. Rev. B* **87** 125124
[11] Markiewicz R S, Sahrakorpi S, Lindroos M, Lin H and Bansil A 2005 *Phys. Rev.* B **72** 054519
[12] Shastry B S and Shraiman B 1990 *Phys. Rev. Lett.* **65** 1068
[13] Ando Y 2007 *High Tc Superconductors and Related Transition Metal Oxides* ed A Bussman-Holder and H Keller (Berlin: Springer)
[14] Ando Y, Boebinger G S, Passner A, Kimura T and Kishio K 1995 *Phys. Rev. Lett.* **74** 3253
[15] Ando Y, Komiya S, Segawa K, Ono S and Kurita Y 2004 *Phys. Rev. Lett.* **93** 267001
[16] Martin S, Fiory A T, Fleming R M, Schneemeyer L F and Waszczak J V 1988 *Phys. Rev.* B **60** 2194
[17] Takagi H, Ido T, Ishibashi S, Uota M, Uchida S and Tokura Y 1989 *Phys. Rev.* B **40** 2254
[18] Onose Y, Taguchi Y, Ishizaka K and Tokura Y 2004 *Phys. Rev.* B **69** 024504
[19] Li Y, Tabis W, Yu G, Barišić N and Greven M 2016 *Phys. Rev. Lett.* **117** 197001
[20] Voruganti P, Golubentsev A and John S 1992 *Phys. Rev.* B **45** 13945
Fukuyama H, Ebisawa H and Wada Y 1969 *Prog. Theor. Phys.* **42** 494
Kohno H and Yamada K 1988 *Prog. Theor. Phys.* **80** 623
[21] Arsenault L-F and Tremblay A M S 2013 *Phys. Rev.* B **88** 205109
[22] Chien T R, Wang Z Z and Ong N P 1991 *Phys. Rev. Lett.* **67** 2088
[23] Ong N P and Anderson P W 1997 *Phys. Rev. Lett.* **78** 977
[24] Ding W, Žitko R and Shastry B S 2017 *Phys. Rev. B* **95** 115153
[25] Ando Y, Kurita Y, Komiya S, Ono S and Segawa K 2004 *Phys. Rev. Lett.* **92** 197001
[26] Hwang H Y, Batlogg B, Takagi H, Kao H L, Kwo J, Cava R J, Krajewski J J and Peck W F Jr. 1994 *Phys. Rev. Lett.* **72** 2636
[27] Balakirev F F, Betts J B, Migliori A, Tsukada I, Ando Y and Boebinger G S 2009 *Phys. Rev. Lett.* **102** 017004
[28] Takeda J, Nishikawa T and Sato M 1994 *Physica* C **231** 293
[29] Town J *et al* 2014 XSEDE: accelerating scientific discovery *Comput. Sci. Eng.* **16** 62–74
[30] Hansen D and Shastry B S 2013 *Phys. Rev.* **87** 245101